

pubs.acs.org/NanoLett Letter

Hot Carrier Thermalization and Josephson Inductance Thermometry in a Graphene-Based Microwave Circuit

Raj Katti,[#] Harpreet Singh Arora,[#] Olli-Pentti Saira,[#] Kenji Watanabe, Takashi Taniguchi, Keith C. Schwab, Michael Lee Roukes, and Stevan Nadj-Perge*



Cite This: Nano Lett. 2023, 23, 4136-4141



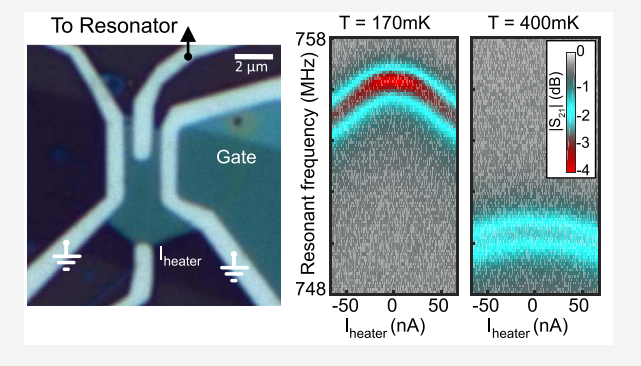
ACCESS I

III Metrics & More

Article Recommendations

Supporting Information

ABSTRACT: Due to its exceptional electronic and thermal properties, graphene is a key material for bolometry, calorimetry, and photon detection. However, despite graphene's relatively simple electronic structure, the physical processes responsible for the heat transport from the electrons to the lattice are experimentally still elusive. Here, we measure the thermal response of low-disorder graphene encapsulated in hexagonal boron nitride by integrating it within a multiterminal superconducting microwave resonator. The device geometry allows us to simultaneously apply Joule heat power to the graphene flake while performing calibrated readout of the electron temperature. We probe the thermalization rates of both electrons and holes with high precision and observe a thermalization scaling exponent not consistent with cooling through the graphene bulk and argue that instead it can be



attributed to processes at the graphene—aluminum interface. Our technique provides new insights into the thermalization pathways essential for the next-generation graphene thermal detectors.

KEYWORDS: graphene, superconducting devices, thermalization, electron-phonon coupling

raphene provides a tantalizing opportunity for the design I and development of bolometric detectors, due to its exceedingly small heat capacity, 1,2 much smaller compared to traditionally synthesized thin films. In addition, the thermal conductivity of graphene can be greatly changed by coupling it to superconducting or normal electrodes or placing it on different substrates. Moreover, when graphene is contacted using superconducting electrodes, the resulting Josephson coupling and the corresponding supercurrents are highly dependent on electron temperature.³ Accordingly, graphenebased Josephson junctions (gJJs) are particularly promising for detecting ultrasmall thermal responses at milli-Kelvin temperatures. In turn, gJJs can be tuned in many ways, as graphene couples well with a variety of superconductors to form highly transparent junctions, enabling supercurrents to persist over several microns.^{4,5} Using different superconductors, junction geometry, and operation at different carrier densities allows, in principle, for a range of specific optimizations needed for detecting small heat and optical signals. To achieve the highest sensitivity, for example, one can choose to operate at the lowest temperatures and employ superconductors with a small superconducting gap, similar to the approach that is taken in conventional superconducting nanowire-based detectors. If a large dynamic range is required, tuning the critical currents in graphene junctions by controlling carrier density can provide additional flexibility in design.

Despite the significant progress in integrating graphene with superconducting nanoelectronic devices, the present understanding of the thermalization of electrons and holes in these systems is still incomplete. In most transport measurements performed to date, thermalization in gJJs is thought to be primarily driven by the electron-phonon interaction in graphene bulk, as the diffusion of unpaired electrons into the metallic leads is suppressed due to the superconducting gap. However, in the case where graphene is encapsulated within boron nitride (hBN), deduced values of electronphonon coupling from the experimental thermalization rates⁸ are typically orders of magnitude larger than theoretical predictions. Such a discrepancy is not expected for materials with a simple band structure such as graphene, where both the electronic and phonon spectrum can be readily calculated. Further, recent scanning SQUID experiments, which provide spatially resolved thermal imaging of graphene, have revealed that, when electronic transport in graphene is ballistic, signatures of electron thermalization are present only near

Received: December 9, 2022 Revised: May 5, 2023 Published: May 10, 2023





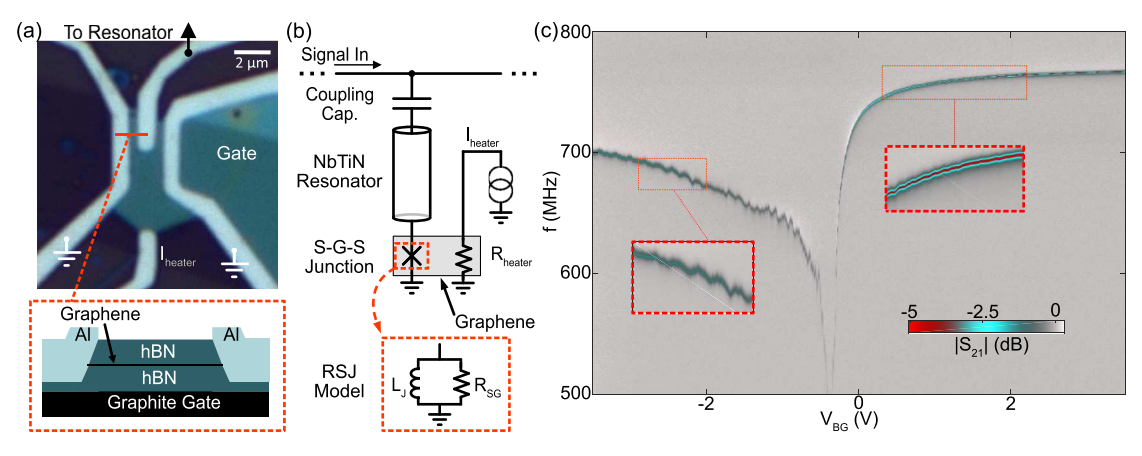


Figure 1. Graphene Josephson junction and the characterization of the resonator circuit. (a) Optical image showing a top-down view of the graphene flake encapsulated in hexagonal boron nitride (blue-green) contacted by superconducting electrodes (light blue). The top contact is placed in close proximity to the ground wires to form the graphene Josephson junction (gJJ). The bottom contact placed far from the ground electrodes is used to apply Joule heating. The inset shows the partial cross-section across the gJJ. Tuning the global carrier density in the graphene flake is achieved by applying a DC voltage $V_{\rm BG}$ to a graphite backgate. (b) Simplified electrical circuit schematic (for full schematic, see Supporting Information, Section S2). A superconducting niobium titanium nitride (NbTiN) resonator is coupled to the external microwave line via a coupling capacitor and terminated by the gJJ. The gJJ is electrically modeled as the parallel sum of a dissipationless branch of inductance $L_{\rm J} = \frac{\Phi_0}{2\pi l_c}$ and a dissipative branch of resistance $R_{\rm SG}$. A dedicated heater port allows application of Joule heat to the graphene flake. (c) $|S_{21}|$ vs $V_{\rm BG}$ shows the evolution of the resonance feature. Near the charge neutrality point (CNP; $V_{\rm CNP} = -0.3$ V), the gJJ maximally loads the resonant requency. On the hole side $(V_{\rm BG} < V_{\rm CNP})$, Fabry—Perot type oscillations are visible due to the formation of the regions of different doping in the bulk graphene (hole doping; p-type) and in the vicinity of contacts (electron doping; n-type).

physical edges, near local defects, and close to metallic contacts. However, signatures of such boundary-mediated thermalization have so far not been evident in transport measurements. Here we present thermal measurements of a device architecture in which graphene temperature is measured via changes in Josephson inductance ¹⁰ caused by heating. In contrast to typical critical current measurements that involve switching between superconducting and resistive states, this approach allows us to continuously monitor thermal response with high precision that, in principle, depends only on the measurement integration time. Surprisingly, for both electron and hole doping, we observe the temperature dependence of the thermal conductance, consistent with a resonant electronic scattering mechanism^{11,12} that occurs at the interface between graphene and superconducting leads.

Figure 1 shows a schematic of the device architecture and basic characterization measurements. A gJJ is integrated into a graphene flake of approximate area $A = 25 \mu \text{m}^2$ (Figure 1(a)). The gJJ consists of a central superconducting contact separated from two symmetrically placed superconducting contacts shorted to the ground plane. Connection is made at the other end of the flake to a heater port used for thermal characterization (see Supporting Information, sections S1 and S2 for details of device fabrication and the measurement architecture). Superconducting aluminum is used for all contacts as it has a small gap relative to other elemental superconductors; we expect this will maximize temperature sensitivity in the sub-Kelvin temperature range of our measurements. To probe the response of the gJJ supercurrent to changes in electron density and temperature, we couple it to an on-chip resonator^{6,13} (Figure 1(b)). Since the gJJ acts as an additional inductive element, it modifies the resonant frequency, which we monitor through microwave reflectometry. The parameters characterizing the gJJ, the Josephson inductance $L_{\rm J}=\frac{\Phi_0}{2\pi I_c}$ and subgap resistance $R_{\rm SG}$, depend

strongly on electron density (see also Supporting Information, section S5). Accordingly, the resonant frequency and spectral width are both highly dependent on the back gate voltage $V_{\rm BG}^{\ \ \ \ \ }$ (Figure 1(c)). Note that we can resolve the resonance over a large range of gate voltages; this allows us to study phenomena arising from electron and hole doping as well as near charge neutrality ($V_{\rm BG}\approx -0.4~\rm V$). For hole doping ($V_{\rm BG}<-0.4~\rm V$), Fabry–Perot-type oscillations indicate that carrier transport is ballistic in our high-quality graphene sample.

In addition to the electrostatic doping, the circuit resonance is also strongly dependent upon temperature (Figure 2). When the device temperature increases, the resonance dip shifts to lower frequencies and broadens, reflecting increased losses occurring within the junction. Importantly, the observed shape of the resonance can be fitted using a standard four-parameter Lorentzian fit function at all accessible carrier densities (2.2 × $10^{12}~{\rm holes/cm^2}$ < $n_{\rm carrier}$ < 5.5 × $10^{11}~{\rm electrons/cm^2})$ and temperatures (160 mK < $T_{\rm mxc}$ < 480 mK) (see also Supporting Information, section S3). The high level of agreement between data and the fit (Figure 2(a)) allows us to relate the deduced resonance parameters to the physical properties of the junction. In particular, shifts of resonant frequency f_0 and the overall resonance shape, which are set by the internal quality factor Qi, can be related to parameters of the resistively shunted junction (RSJ) model, 14 the gJJ critical current I_{c} and subgap resistance $R_{\rm SG}^{6}$ (see Figure 1(b) and Supporting Information, section S5). These quantities determine the small-signal electrical response of the junction at any temperature and doping level. We note that an estimate of microwave losses in the junction is not accessible from the switching current measurements that have typically been employed in gJJ threshold detection schemes. Fitting the temperature dependence of $I_c(T)$ allows the estimation of an induced superconducting gap $\Delta \sim 80 \mu eV$ (see Supporting Information, section S6). Finally, since we expect the resonator

Nano Letters pubs.acs.org/NanoLett Lette

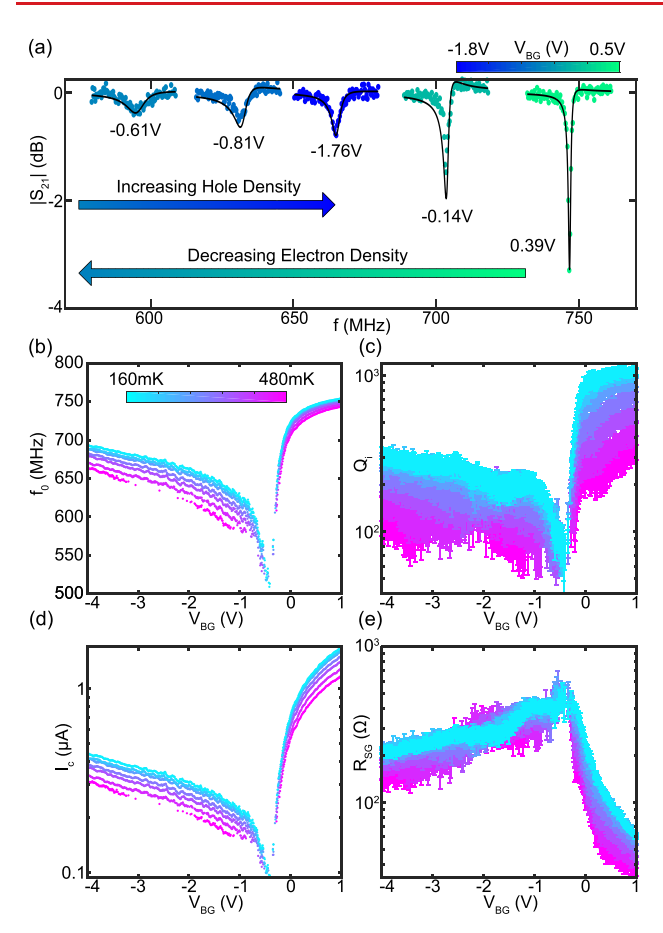


Figure 2. Resonance fits and extracted parameters. (a) Representative $|S_{21}|$ data and fits for electron and hole doping. Color and labels denote backgate voltage $V_{\rm BG}$. Arrows show the direction of resonant frequency shifts as V_{BG} is swept from positive voltage (electron doped) to negative voltage (hole doped) through charge neutrality. Green arrow shows the resonant frequency approaching 500 MHz as electron doping decreases to charge neutrality. Blue arrow shows that the resonant frequency increasing away from 500 MHz as hole doping increases. (b) f_0 as a function of V_{BG} for representative $T_{mxc} = 160$, 210, 260, 310, 360, 410, and 460 mK. Extracted resonant frequency f_0 as a function of $V_{\rm BG}$ shows a characteristic line shape consistent with Figure 1(c). As T_{mxc} increases, f_0 decreases for all backgate voltages. (c) $Q_{\rm i}$ as a function of $V_{\rm BG}$ and $T_{\rm mxc}$ (d, e) RSJ model parameters $I_{\rm c}$ (d) and R_{SG} (e) as a function of V_{BG} and T_{mxc} . I_c and R_{SG} are determined using a numerical impedance model of the resonator/gJJ device with resonance parameters (f_0, Q_i) as inputs (see Figure S3).

ringdown time τ to be the limiting time constant in our device, we estimate from the fitted resonance parameters that $\tau < 150$ ns for all backgate voltages (see Figure S3).

To characterize the thermal properties of the gJJ device, we employ a measurement configuration in which the gJJ is heated internally by applying a DC current $I_{\rm heater}$ to the heater port (Figure 3). The port electrode is placed sufficiently far from the ground electrodes to preclude supercurrent flow. This configuration allows us to accurately monitor the input power delivered to the graphene flake while simultaneously monitoring the resonance frequency. For different device temperatures and doping, representative changes in the S_{21} resonance dip are shown in Figure 3(a-c) and Figure 3(f-h). By increasing the stage temperature from 170 mK to 400 mK, we observe a decrease in the resonant frequency of 27 MHz for holes, compared to 6 MHz for electrons. This is consistent

with greater inductive loading (lower I_c) in the hole regime (see Supporting Information, section S5). By applying a heater current I_{heater} , the internal flake temperature T is increased above T_{mxc} decreasing the resonant frequency. Combined with the measurements taken at different temperatures for calibration (Figure 3(e,j)) the power vs temperature characterization and, consequently, the thermal conductivity G_{th} of the graphene flake can be determined. Note that at given heater powers and temperatures corresponding to the same resonant frequency the mesured Q-factors are also nearly identical (within the experimental error). While the presence of nonthermal quasiparticles can be detected in the experiment, the observations of matching Q-factors and resonant frequencies in two scenarios ensure that the system is not too far from thermal equilibrium. We use this approach to investigate thermal properties for both electron and hole doping regimes.

The data we have acquired is consistent with a power law $P_{heater} = \Sigma A(T^n - T_{mxc}^n)$, with electron temperature T, stage temperature T_{mxc} , scaling exponent n, and the electronphonon coupling prefactor ΣA (see also Supporting Information, section S7). We plot $\partial P/\partial T = G_{\text{th}} = n\Sigma AT^{n-1}$ (Figure 4(c)) which shows that the scaling exponents for hole and electron doping are consistent with n = 5. We note that our fitting procedures produce only comparably small errors for each of the individual data points, and accordingly, the uncertainty of the extracted scaling exponent is much less than 1. This enables us to clearly distinguish that the exponent obtained here is *not* consistent with the n = 3 or n = 4 scaling predicted for bulk electron-phonon coupling in reduced dimensions. 15,16 While an n = 5 scaling exponent is expected for the electron—phonon coupling of a 3D electron gas, ¹⁷ these considerations do not apply for our graphene device in which the electron and phonon density-of-states are 2D. Also, we note that the mechanism where hot electrons (or holes) diffuse into the superconducting aluminum leads before thermalization, while in principle possible, is not consistent with our observations (see Supporting Information, section S8 for a more detailed discussion).

Measurements of hBN-encapsulated graphene performed previously^{5,8} reveal that G_{th} (scaled by the area) is about three orders of magnitude larger than predictions by simple bulk electron—phonon coupling theory. The magnitude of $G_{\rm th} \sim 5$ — 300 pW/K in our measurements is consistent with these observations. Due to enhanced mobility, hBN-encapsulated graphene is typically in the ballistic scattering limit, in which the carrier mean free path l_{mfp} is limited by the device dimension ($L_{\text{device}} \approx 5 \, \mu \text{m}$ in our sample). This observation has led to the hypothesis that the enhanced $G_{\rm th}$ may arise from "resonant supercollisions", 11,12 a scenario consistent with the spatially resolved measurements. 9,18 In this scenario, defects located at the edge of the graphene flake locally enhance electron-phonon interactions and open a thermalization pathway that dominates over electron-phonon coupling in the bulk. Spatially resolved scanning SQUID measurements show an enhancement of surface phonon temperature at graphene edges and close to metal contacts. The theory formulated to explain these results¹² suggests that an n = 5scaling exponent should hold down to milli-Kelvin temperatures ($T < T_{BG}$) in the limit of strong scattering ($\delta \sim 1$). In this context, our high precision measurements of the n = 5scaling exponent are in principle consistent with the possibility of such supercollisions being the dominant thermalization

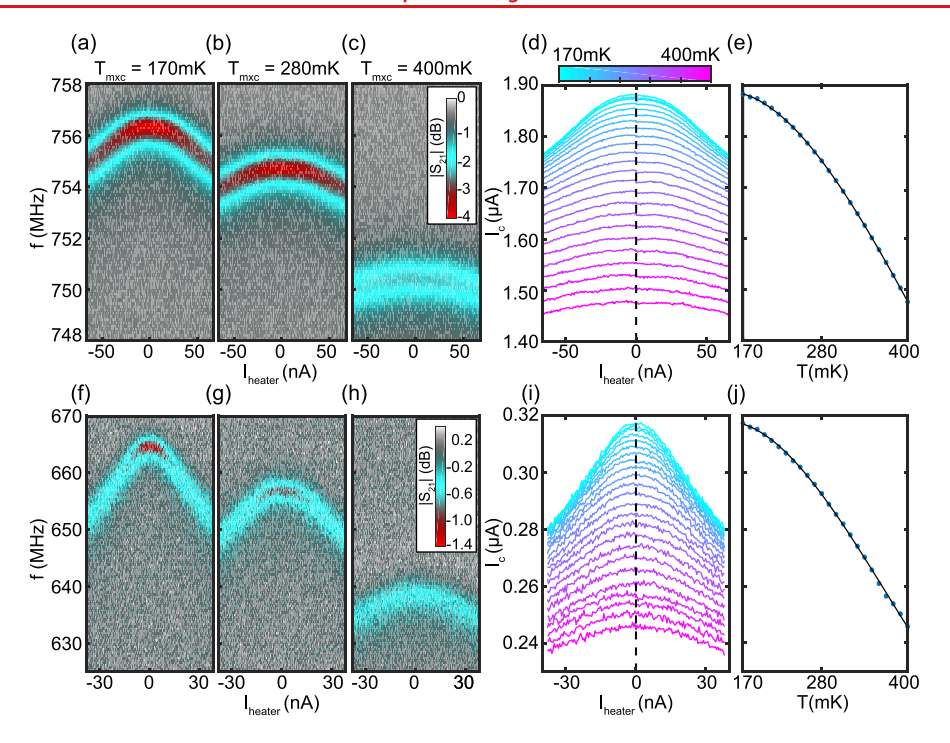


Figure 3. Electron-side and hole-side heating and calibration. (a–c) Electron-side ($V_{\rm BG}=1.1~\rm V$) and (f–h) hole-side ($V_{\rm BG}=-1.8~\rm V$) $|S_{21}(f)|$ vs $I_{\rm heater}$ for three representative mixing stage temperatures (a, f) $T_{\rm mxc}=170~\rm mK$, (b, g) $T_{\rm mxc}=280~\rm mK$, and (c, h) $T_{\rm mxc}=400~\rm mK$. Applying a DC heater current $I_{\rm heater}$ to the designated heater port decreases the resonant frequency of the device. As expected, the shifts are symmetric with respect to the polarity of $I_{\rm heater}$ (d) Electron-side and (i) hole-side $I_{\rm c}$ as a function of $I_{\rm heater}$ for different mixing chamber temperatures. Fitting (a–c) and (f–h) allows extraction of resonance parameters (f_0 , Q_i) and junction parameters (I_c , $R_{\rm SG}$) (see also Supporting Information, section S4). The dashed line at $I_{\rm heater}=0~\rm nA$ corresponds to the data cut plotted in (e) and (j). (e) Electron-side and (j) hole-side calibration curve of the unheated $I_{\rm c}$ as a function of $T_{\rm mxc}$. Since $I_{\rm c}$ monotonically decreases with increasing mixing chamber temperature $T_{\rm mxc}$, there is a one-to-one correspondence between $I_{\rm c}$ and graphene flake temperature.

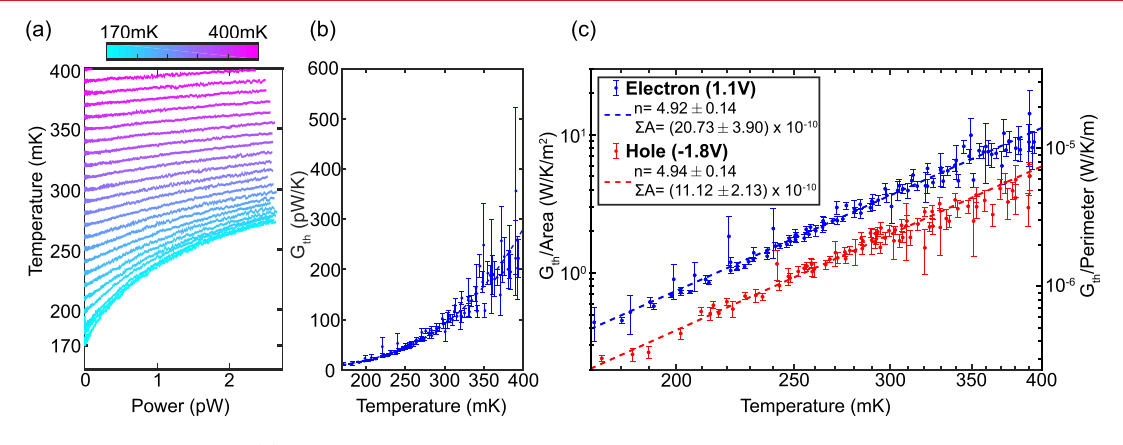


Figure 4. Power—temperature curves. (a) Electron-side flake temperature as a function of heat power. From the injected DC current I_{heater} and measured voltage drop V across the heater port, the injected heater power can be determined: $P_{\text{heater}} = I_{\text{heater}} \times V$. From the I_c vs I_{heater} traces in Figure 3(d,i) and the I_c vs T_{mxc} calibration in Figure 3(e,j), flake temperature can be determined as a function of applied P_{heater} . Color corresponds to the mixing chamber stage temperature. (b) G_{th} vs T_{mxc} . Taking the numerical derivative $\frac{\partial P}{\partial T}$ of Figure 4(a) allows the data to be plotted on a single line. Fit line is to the power law $G_{\text{th}} = \partial P/\partial T = n\Sigma A T^{n-1}$ where n is the scaling exponent and ΣA (in units of W/K^5) is the multiplicative factor. (c) Electron and hole G_{th} vs T_{mxc} (log—log scale). Hole and electron doping both show power law scaling with an n = 5 exponent.

pathway at sub-Kelvin temperatures. We note, however, that a large portion of our graphene edge is contacted with superconducting aluminum, which may significantly alter this simple interpretation. Further exploration of the device parameter space (e.g., sample size, aspect ratio, disorder) and an understanding of the graphene—aluminum interface may be needed to fully disentangle relations between different microscopic thermalization mechanisms in general.

We note that $G_{\rm th}$ exhibits a power law consistent with n=5 for both electron and hole doping, indicating that this mechanism remains dominant in both regimes. Interestingly, the electron- and hole-side prefactors differ by a factor of approximately two (see Figure 4(c)). Inspired by the result in ref 9, a possible explanation for this difference arises from the energy distribution of resonant scattering centers in the bare graphene edge. A potential complication with this explanation

Nano Letters pubs.acs.org/NanoLett Letter

arises from the fact that in our experiment scatterers are in close proximity to aluminum, which as mentioned above may significantly alter their properties. We note that, in the case of hole doping, the intrinsic p-n junction formed between the graphene region close to the Al contacts (which is always intrinsically n-doped) and the p-doped bulk may also play a role. In this scenario, holes from the bulk must pass across the p-n junction in order to efficiently thermalize. Since the p-n junction has a finite transmission probability, it may reduce the overall thermalization rate. Attaining an accurate calculation of the thermalization prefactor from the first-principles is difficult due to the effects outlined above, and further theoretical and experimental work is needed for quantitative comparisons. For example, tracing out evolution of $G_{\rm th}$ as a function of electron density near charge neutrality may help disentangle various reasons for the observed difference between electron and hole thermalization.

In the context of detector technologies, graphene is argued to be a promising platform for future scalable far-infrared or microwave detector arrays. 8,19 Its utility for this purpose is typically evaluated on the basis of optimization of several key attributes including response time, responsivity, thermal insulation, and multiplexing that, in turn, require simultaneous optimization of multiple device parameters. The hBNencapsulated graphene devices studied here provide large supercurrents and submicrosecond response times that allow for continuous monitoring of thermal response and integration of the resonator readout that permits straightforward frequency-division multiplexing of many devices on a single feedline. 20,21 Moreover, in our scheme the presence of a separate heater port can be employed for broad-spectrum energy detection. We note that a thermal insulation of the architecture employed here can be achieved at the expense of lowering the mobility in graphene by, for example, placing it directly on the oxide substrate 19 instead of hBN.

Finally, we briefly compare the inductance readout scheme employed here with graphene detectors based on junction switching^{8,22} (between the zero and finite voltage state) as their potential applications may significantly differ. The latter type of detector registers a "count" when the incident photon energy is above a given threshold and therefore forfeits the possibility of energy spectroscopy provided by the linear, resonantly coupled graphene detector architecture pursued in this work. Further, threshold detectors intrinsically provide a slower response, which is limited by the cooling and resetting of the junction after a photon absorption event. While this type of detector may be a desirable option in experiments where photon energy and arriving time are known or controlled, the inductance readout detection scheme is more suitable for novel spectroscopy applications of unknown sources, ²³ including dark matter detection ^{24–27} and photon and phonon counting ²⁸ where linear response and ability to fully evaluate detection performance are important (see Supporting Information, section S9 for noise equivalent power characterization).

ASSOCIATED CONTENT

Supporting Information

The Supporting Information is available free of charge at https://pubs.acs.org/doi/10.1021/acs.nanolett.2c04791.

Details of sample fabrication, S21 measurements, fitting procedures, and additional discussion of thermalization pathways and measured noise equivalent power (PDF)

AUTHOR INFORMATION

Corresponding Author

Stevan Nadj-Perge — T. J. Watson Laboratory of Applied Physics, California Institute of Technology, Pasadena, California 91125, USA; ⊚ orcid.org/0000-0002-2394-9070; Email: s.nadj-perge@caltech.edu

Authors

Raj Katti – Department of Physics, California Institute of Technology, Pasadena, California 91125, USA

Harpreet Singh Arora — T. J. Watson Laboratory of Applied Physics, California Institute of Technology, Pasadena, California 91125, USA

Olli-Pentti Saira — Department of Physics and Institute for Quantum Information and Matter, California Institute of Technology, Pasadena, California 91125, USA; Brookhaven National Laboratory, Upton, New York 11973, USA

Kenji Watanabe — National Institute for Materials Science, Tsukuba, Ibaraki 305 0044, Japan; orcid.org/0000-0003-3701-8119

Takashi Taniguchi — National Institute for Materials Science, Tsukuba, Ibaraki 305 0044, Japan; [™] orcid.org/0000-0002-1467-3105

Keith C. Schwab – Department of Physics, California Institute of Technology, Pasadena, California 91125, USA
Michael Lea Poules, Department of Physics, California

Michael Lee Roukes — Department of Physics, California Institute of Technology, Pasadena, California 91125, USA; orcid.org/0000-0002-2916-6026

Complete contact information is available at: https://pubs.acs.org/10.1021/acs.nanolett.2c04791

Author Contributions

*These authors contributed equally to this work.

Notes

The authors declare no competing financial interest.

ACKNOWLEDGMENTS

We acknowledge useful discussions with Sophie Li, Matt Matheney, Ewa Rej, and Jonas Zmuidzinas. This work was supported by NSF through the program CAREER DMR-1753306 and Gist-Caltech memorandum of understanding. S.N.-P. also acknowledges the support of the DOE-QIS program (DE-SC0019166), IQIM (NSF-funded physics frontiers center), and the Sloan foundation. M.L.R. acknowledges support from NSF grant NSF-DMR-1806473.

REFERENCES

- (1) Fong, K. C.; Schwab, K. C. Ultrasensitive and Wide-Bandwidth Thermal Measurements of Graphene at Low Temperatures. *Physical Review X* **2012**, *2*, 031006.
- (2) Fong, K. C.; Wollman, E. E.; Ravi, H.; Chen, W.; Clerk, A. A.; Shaw, M. D.; Leduc, H. G.; Schwab, K. C. Measurement of the Electronic Thermal Conductance Channels and Heat Capacity of Graphene at Low Temperature. *Physical Review X* **2013**, *3*, 041008.
- (3) Borzenets, I. V.; Amet, F.; Ke, C. T.; Draelos, A. W.; Wei, M. T.; Seredinski, A.; Watanabe, K.; Taniguchi, T.; Bomze, Y.; Yamamoto, M.; Tarucha, S.; Finkelstein, G. Ballistic Graphene Josephson Junctions from the Short to the Long Junction Regimes. *Phys. Rev. Lett.* **2016**, *117*, 237002.
- (4) Calado, V. E.; Goswami, S.; Nanda, G.; Diez, M.; Akhmerov, A. R.; Watanabe, K.; Taniguchi, T.; Klapwijk, T. M.; Vandersypen, L. M. K. Ballistic Josephson Junctions in Edge-Contacted Graphene. *Nat. Nanotechnol.* **2015**, *10*, 761–764.

Nano Letters pubs.acs.org/NanoLett Letter

- (5) Draelos, A. W.; Wei, M.-T.; Seredinski, A.; Li, H.; Mehta, Y.; Watanabe, K.; Taniguchi, T.; Borzenets, I. V.; Amet, F.; Finkelstein, G. Supercurrent Flow in Multiterminal Graphene Josephson Junctions. *Nano Lett.* **2019**, *19*, 1039–1043.
- (6) Schmidt, F. E.; Jenkins, M. D.; Watanabe, K.; Taniguchi, T.; Steele, G. A. A Ballistic Graphene Superconducting Microwave Circuit. *Nat. Commun.* **2018**, *9*, 4069.
- (7) Borzenets, I. V.; Coskun, U. C.; Mebrahtu, H. T.; Bomze, Y. V.; Smirnov, A. I.; Finkelstein, G. Phonon Bottleneck in Graphene-Based Josephson Junctions at Millikelvin Temperatures. *Phys. Rev. Lett.* **2013**, *111*, 027001.
- (8) Lee, G.-H.; Efetov, D. K.; Jung, W.; Ranzani, L.; Walsh, E. D.; Ohki, T. A.; Taniguchi, T.; Watanabe, K.; Kim, P.; Englund, D.; Fong, K. C. Graphene-Based Josephson Junction Microwave Bolometer. *Nature* **2020**, *586*, 42–46.
- (9) Halbertal, D.; Shalom, M. B.; Uri, A.; Bagani, K.; Meltzer, A. Y.; Marcus, I.; Myasoedov, Y.; Birkbeck, J.; Levitov, L. S.; Geim, A. K.; Zeldov, E. Imaging Resonant Dissipation from Individual Atomic Defects in Graphene. *Science* **2017**, *358*, 1303–1306.
- (10) Saira, O.-P.; Zgirski, M.; Viisanen, K. L.; Golubev, D. S.; Pekola, J. P. Dispersive Thermometry with a Josephson Junction Coupled to a Resonator. *Physical Review Applied* **2016**, *6*, 024005.
- (11) Kong, J. F.; Levitov, L.; Halbertal, D.; Zeldov, E. Resonant Electron-Lattice Cooling in Graphene. *Phys. Rev. B* **2018**, 97, 245416.
- (12) Tikhonov, K. S.; Gornyi, İ. V.; Kachorovskii, V. Y.; Mirlin, A. D. Resonant Supercollisions and Electron-Phonon Heat Transfer in Graphene. *Phys. Rev. B* **2018**, *97*, 085415.
- (13) Wang, J. I.-J.; et al. Coherent Control of a Hybrid Superconducting Circuit Made with Graphene-Based van Der Waals Heterostructures. *Nat. Nanotechnol.* **2019**, *14*, 120–125.
- (14) Tinkham, M. Introduction to Superconductivity; Dover Publications, 2004.
- (15) Viljas, J. K.; Heikkilä, T. T. Electron-Phonon Heat Transfer in Monolayer and Bilayer Graphene. *Phys. Rev. B* **2010**, *81*, 245404.
- (16) Chen, W.; Clerk, A. A. Electron-Phonon Mediated Heat Flow in Disordered Graphene. *Phys. Rev. B* **2012**, *86*, 125443.
- (17) Roukes, M. L.; Freeman, M. R.; Germain, R. S.; Richardson, R. C.; Ketchen, M. B. Hot Electrons and Energy Transport in Metals at Millikelvin Temperatures. *Phys. Rev. Lett.* **1985**, *55*, 422–425.
- (18) Halbertal, D.; Cuppens, J.; Shalom, M. B.; Embon, L.; Shadmi, N.; Anahory, Y.; Naren, H. R.; Sarkar, J.; Uri, A.; Ronen, Y.; Myasoedov, Y.; Levitov, L. S.; Joselevich, E.; Geim, A. K.; Zeldov, E. Nanoscale Thermal Imaging of Dissipation in Quantum Systems. *Nature* **2016**, *539*, 407–410.
- (19) Kokkoniemi, R.; Girard, J.-P.; Hazra, D.; Laitinen, A.; Govenius, J.; Lake, R. E.; Sallinen, I.; Vesterinen, V.; Partanen, M.; Tan, J. Y.; Chan, K. W.; Tan, K. Y.; Hakonen, P.; Möttönen, M. Bolometer Operating at the Threshold for Circuit Quantum Electrodynamics. *Nature* **2020**, *586*, 47–51.
- (20) Day, P. K.; LeDuc, H. G.; Mazin, B. A.; Vayonakis, A.; Zmuidzinas, J. A Broadband Superconducting Detector Suitable for Use in Large Arrays. *Nature* **2003**, 425, 817–821.
- (21) Wandui, A.; Bock, J. J.; Frez, C.; Hollister, M.; Minutolo, L.; Nguyen, H.; Steinbach, B.; Turner, A.; Zmuidzinas, J.; O'Brient, R. Thermal Kinetic Inductance Detectors for Millimeter-Wave Detection. *J. Appl. Phys.* **2020**, *128*, 044508.
- (22) Walsh, E. D.; Efetov, D. K.; Lee, G.-H.; Heuck, M.; Crossno, J.; Ohki, T. A.; Kim, P.; Englund, D.; Fong, K. C. Graphene-Based Josephson-Junction Single-Photon Detector. *Physical Review Applied* **2017**, *8*, 024022.
- (23) Lara-Avila, S.; Danilov, A.; Golubev, D.; He, H.; Kim, K. H.; Yakimova, R.; Lombardi, F.; Bauch, T.; Cherednichenko, S.; Kubatkin, S. Towards Quantum-Limited Coherent Detection of Terahertz Waves in Charge-Neutral Graphene. *Nature Astronomy* **2019**, *3*, 983–988.
- (24) Hochberg, Y.; Kahn, Y.; Lisanti, M.; Tully, C. G.; Zurek, K. M. Directional Detection of Dark Matter with Two-Dimensional Targets. *Physics Letters B* **2017**, *772*, 239–246.

- (25) Kim, D.; Park, J.-C.; Fong, K. C.; Lee, G.-H. Detecting keV-Range Super-Light Dark Matter Using Graphene Josephson Junction. 2002.07821. ArXiv. 2020, https://arxiv.org/abs/2002.07821.
- (26) McAllister, B. T.; Flower, G.; Ivanov, E. N.; Goryachev, M.; Bourhill, J.; Tobar, M. E. The ORGAN Experiment: An Axion Haloscope above 15 GHz. *Physics of the Dark Universe* **2017**, *18*, 67–72
- (27) Baracchini, E. PTOLEMY: A Proposal for Thermal Relic Detection of Massive Neutrinos and Directional Detection of MeV Dark Matter. 1808.01892. ArXiv. 2018, https://arxiv.org/abs/1808.01892.
- (28) Roukes, M. L. Yoctocalorimetry: Phonon Counting in Nanostructures. *Physica B: Condensed Matter* **1999**, 263–264, 1–15.